

Hybrid Photothermal Pyroelectric and Thermogalvanic Generator for Multisituation Low Grade Heat Harvesting

Tianpeng Ding, Liangliang Zhu, Xiao-Qiao Wang, Kwok Hoe Chan, Xin Lu, Yin Cheng, and Ghim Wei Ho*

Harvesting of prevalent low grade solar heat from otherwise wasted energy has received tremendous attention. However, extensive and continuous conversion remains challenging due to distributed nature of heat, limited temperature difference with the surroundings, ambient solar heat fluctuation, and night time period of darkness. Herein, a hybrid thermogalvanic and pyroelectric generator for multisituation structured/unstructured, static/dynamic, and day/night waste heat harnessing for continuous operation is reported. Powered by versatile thermal energy harvesting strategies, the hybrid photothermal generator is able to provide a more resilient and adaptive energy system to meet diversified energy demand, irrespective of unpredictable conditions. Taking advantage of the superior photothermal properties and electrical conductivity of carbon nanotubes/cellulose nanocrystals nanocomposite, together with the heat localization effect induced by sponge-confined electrolyte, simultaneous high thermogalvanic and pyroelectric performance is achieved with maximum outputs of 1.86 and 0.9 mW m⁻², respectively. Moreover, a scaled-up hybrid photothermal generator is successfully deployed on both land and water surfaces under natural sunlight, and also the feasibility of nighttime operation is verified. Such hybrid photothermal generators presented here offer an all-day clean energy solution as well as a feasible and cost-effective alternative to capitalize on solar energy and blue energy.

1. Introduction

Solar power is intermittent, and is oftentimes nondispatchable because of variability in cloud cover and limited daylight

Dr. T. P. Ding, Dr. L. L. Zhu, Dr. X.-Q. Wang, K. H. Chan, X. Lu,
Dr. Y. Cheng, Prof. G. W. Ho
Department of Electrical and Computer Engineering
National University of Singapore
4 Engineering Drive 3, Singapore 117583, Singapore
E-mail: elehgw@nus.edu.sg

Prof. G. W. Ho
Engineering Science Programme
National University of Singapore
9 Engineering Drive 1, Singapore 117575, Singapore

Prof. G. W. Ho
Institute of Materials Research and Engineering
A*STAR (Agency for Science, Technology and Research)
3 Research Link, Singapore 117602, Singapore

 The ORCID identification number(s) for the author(s) of this article can be found under <https://doi.org/10.1002/aenm.201802397>.

DOI: 10.1002/aenm.201802397

operation. Seemingly, the intermittency issue can be circumvented, by alternatively intercepting and capturing of solar thermal energy fluxes. Moreover, low grade solar thermal harvesting has attracted significant interest because of its versatility in numerous applications such as steam generation,^[1–5] photo/electrocatalysis,^[6–12] energy harvesters,^[13–17] and actuators.^[18–24] Also, harvesting of ubiquitous low grade waste heat is presently perceived as a promising energy source toward decarbonized and sustainable ecology.

Thermoelectric generator and pyroelectric generator, which can convert thermal energy directly into electricity, are the two particularly attractive ways for solar heat utilization, ascribing to their merits, that is, simple structure, no moving parts and devoid of mechanical deformation.^[25–31] Thermoelectric generator harvests energy via the Seebeck effect triggered by static temperature differences, while the pyroelectric generator delivers through the change of spontaneous polarization in response to dynamic temperature fluctua-

tions. However, most conventional thermoelectric generators are based on high-cost and complicated fabrication of solid-state semiconducting materials constricted by physical limitations and rarely, if ever, attempts have been made to hybrid with other types of thermal energy generator. As an alternative to thermoelectric modules, thermocell (also known as thermogalvanic cell) that utilizes the temperature-dependent entropy changes during electron transfer between redox couples and electrodes is a promising method to convert thermal energy to electricity, with the virtues of relatively high Seebeck coefficient, inexpensive and simple fabrication process.^[32–35] Besides, solar thermal effect induced by an unstructured outdoor environment is inevitably accompanied by thermal fluctuations caused by ever-changing weather condition. Such thermal variance has dramatically impeded some thermal devices to reach their maximum attainable performance. Hence, a judicious design and integration of thermogalvanic and pyroelectric generator can critically underpin effective utilization of solar thermal resource by harvesting energy from static temperature difference derived from a constant solar exposure as well as dynamic temperature fluctuations arising from sporadic ambience.

Here, we devise a hybrid photothermal generator consisting of a pyroelectric generator and a thermocell, constituted by lightweight CNT-based nanocomposites that collectively serve as broadband solar absorber and superior thermal/electrical conductive and high electrochemical specific surface area electrodes. The photothermal generator is designed to be synthetically simple, highly adaptive to the solar energy intermittency and variability while keeping the system autonomous and reliable without adding system complexity and costs. High solar absorptance tailored solar absorber nanocomposite readily absorbs light for photothermal-driven pyroelectricity conversion. Meanwhile, effective suppression of superfluous heat losses through heat transmission is achieved by a low thermal emission reticulated sponge containing thermogalvanic electrolyte. By doing this, a large temperature gradient is conserved across the thermogalvanic electrolyte to achieve high thermoelectric performance. Ultimately, a scaled-up hybrid photothermal thermogalvanic/pyroelectric generator is successfully demonstrated to work both on ground and water surfaces, validating the ability of scavenging concurrent static and dynamic solar thermal energy. Furthermore, the feasibility of nighttime operation verifies the ability of the photothermal generator to ceaselessly recover waste ambient heat to further extend its adaptability for day-night energy supply.

2. Results and Discussion

The mechanism of hybrid photothermal generator is schematically depicted in **Figure 1**. Basically, the hybrid generator is an integrated sandwich structure, consisting of two ferroelectric poly (vinylidene difluoride) (PVDF) films and a block of polyurethane (PU) sponge soaked with ferric/ferrous chloride solution. Nanocomposite constructed by cross-linked CNTs and CNCs is coated on both sides of the PVDF films, serving as electrodes as well as photothermal absorber. The thermogalvanic electrolyte-soaked sponge is sealed by plexiglass to ensure good contact to the two PVDF films as well as to prevent evaporation and oxidation. When exposed to irradiation, the CNT/CNC composite layer on top PVDF film will absorb and transform light into heat, causing a temperature increase ($dT/dt > 0$) of PVDF

film. Consequently, the dipoles within the PVDF will lose their orientation due to thermal vibration, leading to a decrease in the level of spontaneous polarization, thus resulting in a pyroelectric response. As the temperature gradient across the electrolyte is established, the temperature-dependent redox of ferric/ferrous chloride will induce an electrical potential between the electrodes attached to the opposite sides of the electrolyte, that is, thermocell voltage. When the irradiation ceases or weakens, the top PVDF film cools down ($dT/dt < 0$) and the level of spontaneous polarization will increase as the dipoles regain their orientation, thus generating a reverse pyroelectric response. Meanwhile, the decline in temperature gradient will correspondingly lead to a decrease in thermocell response.

As noted above, the CNT/CNC nanocomposite electrodes are essential parts to the performance of the hybrid generator, which assume the function of light absorber. We use a simple solution casting method to coat CNT/CNC electrodes on the PVDF films. In this study, CNCs of ≈ 200 nm in length and 5 nm diameter were synthesized from cellulose fibers through a simple acid hydrolysis method,^[36] and the details are described in the Experimental Section. The atomic force microscope (AFM) image of the CNCs is shown in Figure S1a (Supporting Information), presenting a rod-shaped structure. Due to the presence of surface charge, the CNCs are uniformly dispersed in water.^[36,37] The dispersion exhibits high stability under ambient condition for more than five months, as shown in Figure S1b (Supporting Information). Benefitting from the surface charges on CNCs and the strong interaction between the cross-linking 1D fibrous structures, the CNTs infiltrated CNCs composite can be homogeneously and stably dispersed in water (Figure S2a, Supporting Information).^[37,38] Subsequently, as-prepared CNT/CNC solution was casted and dried onto a predefined area of a PVDF film (**Figure 2a**). The coated area is extremely dark in contrast to the uncovered transparent part. The cross-section scanning electron microscope (SEM) image (inset in Figure 2a) shows the hybrid CNT/CNC layer with thickness of $17 \mu\text{m}$ on the PVDF film. AFM image and typical top-view SEM image of CNT/CNC (with weight ratio of 4:1) coated PVDF film are shown in Figure 2b and Figure S2b (Supporting Information), respectively, indicating a high-density 1D nanofiber/nanotube network structure. Figure S2c,d

(Supporting Information) shows the high-magnification SEM images of the top and cross-section views of the CNT/CNC layer. Particularly, the mutually reinforced 1D network structure of CNTs and CNCs ensures the resistance of a CNT/CNC-coated PVDF film constant during 10 000 bending test with a bending angle of 90° , as shown in Figure 2c, exhibiting excellent flexibility and mechanical stability. It is worth noting that the interconnected CNTs offer an efficient pathway for electron transfer, endowing the electrodes with good electrical conductivity.

To further investigate the role of CNCs in the composite electrodes, the conductivities of the electrodes with different weight ratios of CNTs and CNCs were measured. Each PVDF film with same effective area of

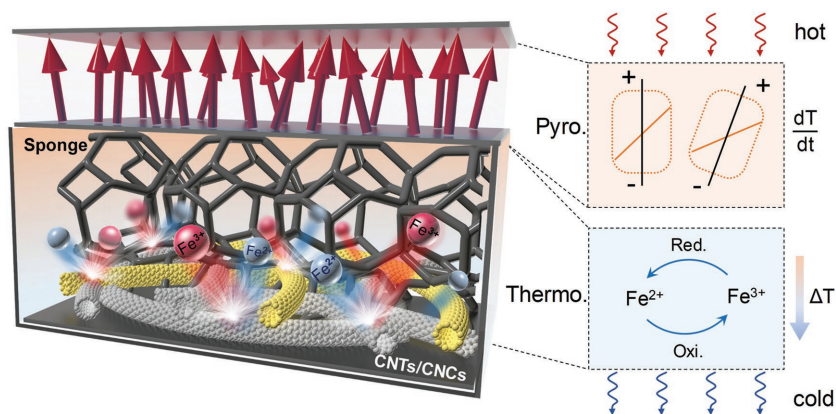


Figure 1. a) Schematic of hybrid photothermal generator. The mechanisms of the photothermal pyroelectric generator (Pyro.) and thermocell (Thermo.) are depicted as upper and lower figures in right, respectively.

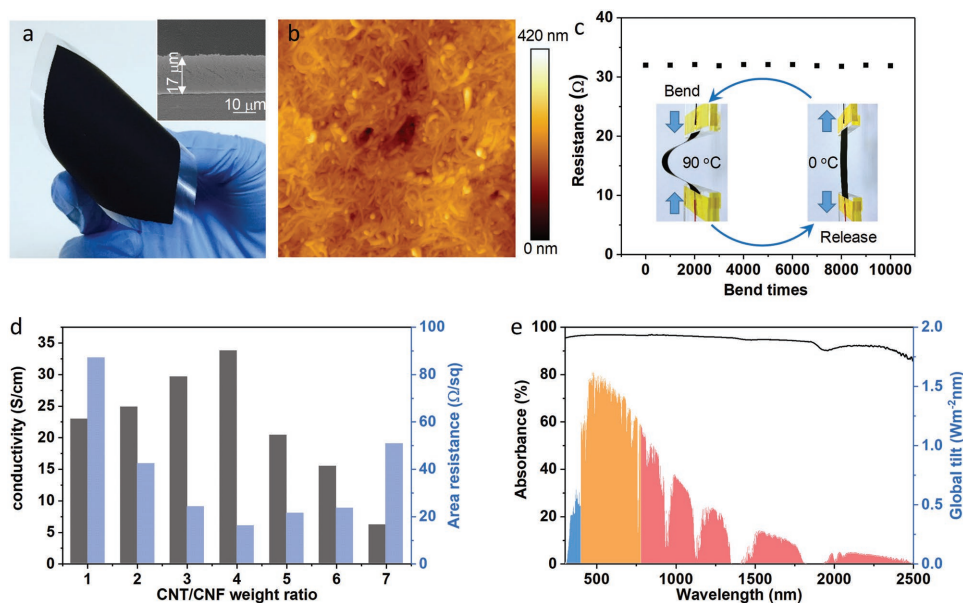


Figure 2. a) Photograph of a PVDF film with CNT/CNC nanocomposite electrodes covered on both sides. Inset is the cross-sectional view of the CNT/CNC electrode. b) AFM image of the CNT/CNC electrode. c) Bending test of a 1 cm × 2 cm CNT/CNC covered PVDF film with a maximum bending angle of 90 °C. The weight ratio of CNT:CNC is 4:1 and the insets are the photos of the film during bending test. d) Conductivity and area resistance of the CNT/CNC electrodes with different weight ratio. e) The absorption spectrum of the CNT/CNC coated PVDF film in the wavelength range from 300 to 2500 nm weighted by standard AM 1.5 G solar spectrum.

1 cm × 1 cm was casted with 200 μL CNT/CNC solution of different weight ratios. As indicated by the histogram in Figure 2d, with the increase of CNTs and CNCs weight ratios from 1:1 to 4:1, the conductivities increase to the highest value of 35 S cm⁻¹ while the area resistances correspondingly decrease to the lowest value of 16 Ω sq⁻¹, which can be ascribed to the increasing current pathway provided by the CNTs. However, further increase in CNTs content will lead to a declining conductivity and rising area resistance. This is mainly due to the aggregation of CNTs when the CNCs ratio in the composites is too low, which validates the crucial role of CNCs in dispersing CNTs as previously reported.^[37]

As excellent light-absorbing materials,^[2,39,40] the CNTs in the nanocomposite not only endow the electrodes with good electrical conductivity but also enable broadband and efficient solar absorption. The absorption spectra of the CNT/CNC nanocomposite (weight ratio of CNT:CNC is 4:1) coated PVDF film in the solar spectrum range across 300–500 nm are shown in Figure 2f, presenting a high overall light absorbance for sunlight with more than 96% weighted by standard air mass 1.5 global (AM 1.5 G) solar spectrum. The superior solar irradiation absorption of the film lays the foundation for an efficient solar-thermal conversion.

To test the performance of the CNT/CNC-coated PVDF films that serve as thermocell electrodes, two pieces of PVDF films coated with CNT/CNC nanocomposite on single side were placed face to face in a rectangular electrolyte tank, as shown in the upper diagram of Figure 3a. The distance between the electrodes was 5 mm and the tank was filled with 0.4 mol L⁻¹ ferric/ferrous chloride aqueous electrolyte solution. When subjected to a temperature difference, temperature-dependent thermogalvanic voltage/current is reliably generated. Figure 3b presents the open-circuit voltage (V_{oc}) and short-circuit current

(I_{sc}) of the thermocell setup at different temperature differences. The thermo-electrochemical Seebeck coefficient is about 1.1 mV K⁻¹, close to previously reported Fe²⁺/Fe³⁺ based thermocell.^[34,41] Due to the high conductivity and specific surface area, the generated thermogalvanic current density reaches 1.2 A m⁻² at a temperature difference of 10 °C.

The photothermal pyroelectric performance of the CNT/CNC-coated PVDF film was also systematically investigated using a setup sketched in the lower diagram of Figure 3a. Figure 3c presents the temperature profiles of the film under different cyclical irradiation time of 60, 30, 20, and 10 s. The intensity of the intermittent solar irradiation is 1000 W m⁻² (AM 1.5 G). When the light on/off duration is kept at 60 s, it can be observed that the temperature of the film increases from 23 to 47 °C in ≈40 s once it is exposed to the light irradiation, and attains steady state when the heat dissipated to ambient and the photothermal conversion reaches an equilibrium. Meanwhile, the PVDF film generates a positive V_{oc} as high as 200 V (upper graph of Figure 3d). On the contrary, when the solar radiation is blocked off, the V_{oc} is reversed to a negative value of about -120 V as the temperature reverts to the room temperature of 23 °C. It is observed that when the on/off period decreases to 30, 20, and 10 s, the highest attainable temperature of the film decreases while the lowest one increases, resulting a decreasing temperature change (ΔT). The functional relation between pyroelectric voltage (V) and temperature change (ΔT) is depicted as follows^[27]

$$V = \frac{pd}{\epsilon_r \epsilon_0} \Delta T \quad (1)$$

where p is the pyroelectric coefficient, d is the thickness of the PVDF film, and ϵ_r and ϵ_0 are the relative and vacuum dielectric

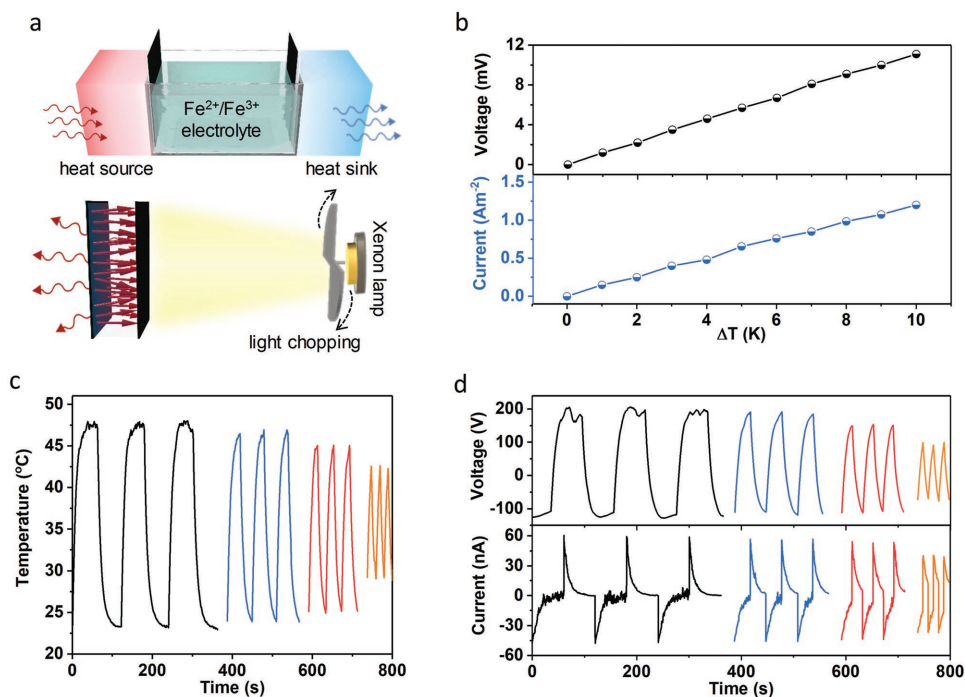


Figure 3. a) Schematics of thermogalvanic (upper) and solar pyroelectric (lower) measurement. b) V_{oc} (upper) and I_{sc} (lower) of the thermocell with CNT/CNC electrodes at different temperature differences. c) Temperature profiles of a CNT/CNC coated PVDF film under different cyclical irradiation time of 60, 30, 20, and 10 s. d) V_{oc} (upper) and I_{sc} (lower) of the PVDF film under different cyclical irradiation time.

constants, respectively. According to Equation (1), the voltage generated via pyroelectric effect will decrease accordingly, which is consistent with the voltage curves in Figure 3d. For a PVDF film with active area of A , the pyroelectric current (I) is expressed as^[27]

$$I = pA \frac{dT}{dt} \quad (2)$$

The temperature change rates ($\frac{dT}{dt}$) of the film can be calculated using the time derivation of the temperature. As shown in Figure S3 (Supporting Information) and lower graph of Figure 3d, a diminishing rate of temperature change and I_{sc} are anticipated as the exposure time decreases. Nonetheless, fully reversible and consistent current output can be obtained upon repeated on/off cycle, even down to a short light switching/intermittency of 10 s.

According to the Seebeck effect, higher temperature difference yields larger potential difference. In the context that solar is used as heat source, the temperature gradient across the device is closely related to the heat transfer capacity of the electrolyte. Porous structure such as aerogels,^[6,42] carbonized polymers,^[43,44] and even woods^[5,45,46] have been widely adopted in steam generation expedition to create confined high temperature region (i.e., heat localization) enabled by their intrinsic low thermal conductivity and high porosity. Similarly, we used polyurethane (PU) sponge, a common cheap porous material to realize heat localization and retention. Figure S4 (Supporting Information) shows a piece of PU sponge soaked with electrolyte, where the electrolyte is fully contained in the porous structure due to the capillary effect. Unlike the conventional smooth, undulated,

and vigorous thermal convection in a free-flowing electrolyte reservoir as shown in the upper diagram of Figure 4a, the thermal convection of a sponge-confined electrolyte is severely hampered by the reticulated boundaries of open cell sponge structures, as shown in the lower diagram of Figure 4a. As such, heat insulation characteristics of the sponge and the constricted convection flow enclosed by the pore boundaries will considerably restrict heat transfer. Thus, superfluous heat loss is effectively suppressed and the heat is localized at the hot zone, favorably conserving a large temperature gradient across the electrolyte. Apart from the interconnected pores in the sponge which provide scaffold for holding electrolyte and channels for ions transportation during redox reaction, importantly they serve to sustain a higher temperature difference.

To experimentally explore the effect of sponge on energy generation, we compare the thermogalvanic and pyroelectric performance between the sponge-confined electrolyte and free-flowing electrolyte hybrid devices. The active areas for these two hybrid devices are kept the same at $2 \text{ cm} \times 2 \text{ cm}$. The bottom of the device was contacted to a heat sink to maintain a room temperature of $\approx 22.8 \text{ }^\circ\text{C}$, while the top surface was exposed to cyclical light irradiation with intensity of 1 sun. The temperature profiles of the devices were recorded by an infrared camera. Figure 4b depicts the typical temperature profiles of the hybrid devices with sponge-confined and free-flowing electrolyte, respectively. Instantaneous rise in temperature can be seen for both devices with the turning on of the light and when the light is turned off, the temperature will decrease to the original dark value. However, it is worth noting that the maximum temperature gradient across the photothermal generator with sponge-confined electrolyte is about $11.2 \text{ }^\circ\text{C}$, almost twice of

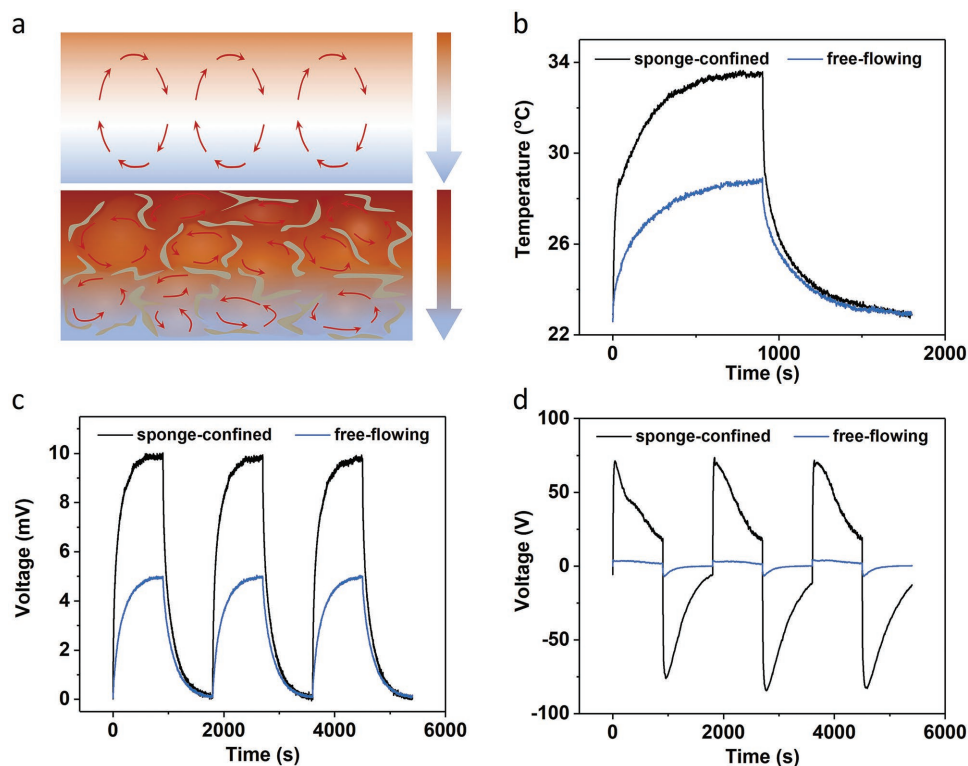


Figure 4. a) Schematic diagrams for thermal convection in free-flowing electrolyte (upper) and sponge-confined electrolyte (lower). b) Temperature profiles for the generators with sponge-confined electrolyte and free-flowing electrolyte. c) V_{oc} of the thermogalvanic generator and d) pyroelectric generator of hybrid generators with sponge-confined and free-flowing electrolyte.

that across the generator with free-flowing electrolyte which is about 6 °C. Figure S5a (Supporting Information) presents the infrared images of the hybrid generators with free-flowing electrolyte (upper) and sponge-confined electrolyte (lower) after 15 min irradiation, visually showing the heat localization achieved via infusion of sponge that substantially limits heat losses. Moreover, the peak value of temperature change rate (dT/dt) for photothermal generator with sponge-confined electrolyte is also higher, with a value of 1.1 $k s^{-1}$ compared to that with free-flowing electrolyte which is around 0.75 $k s^{-1}$ (Figure S5b, Supporting Information).

The thermogalvanic voltage and current change over time for the two hybrid generators is similar to the respective temperature profiles. As shown in Figure 4c and Figure S5c (Supporting Information), both the thermogalvanic V_{oc} and I_{sc} increase in the presence of light illumination, which otherwise would decrease in the absence of illumination. The highest thermogalvanic V_{oc} and I_{sc} generated by the sponge-confined electrolyte device are 10 mV and 0.3 mA, respectively. By contrast, the highest thermogalvanic V_{oc} and I_{sc} generated by

the generator with free-flowing electrolyte reach only 5 mV and 0.28 mA, respectively. The pyroelectric performance of the hybrid generator is also greatly improved when the electrolyte is contained in a sponge. As shown in Figure 4d and Figure S5d (Supporting Information), the pyroelectric V_{oc} and I_{sc} generated by the generator with sponge-confined electrolyte are around 85 V and 17 nA, respectively. In comparison, the pyroelectric V_{oc} and I_{sc} of the generator with free-flowing electrolyte are immensely reduced to 4 V and 9 nA, respectively.

The detailed comparisons between these two types of hybrid generators are listed in Table 1. According to the Seebeck coefficient calculated above, the temperature gradient across the sponge-confined electrolyte is about 9.1 °C. Whereas the highest apparent temperature difference between the top and bottom surface is about 11.2 °C, which is about 2 °C higher than the calculated value. That is because part of the temperature difference across the entire device drops on the top and bottom PVDF substrates. The maximum power output ($1/4V_{oc}I_{sc}$) generated by the thermocell of the hybrid generator with sponge-confined electrolyte is 1.86 $mW m^{-2}$, over two times than

Table 1. Comparisons between the hybrid generators with sponge-confined electrolyte and free-flowing electrolyte. Thermo. and Pyro. represent thermogalvanic and pyroelectric generator, respectively.

Electrolyte	ΔT [°C]	dT/dt [$k s^{-1}$]	Thermo. V_{oc} [mV]	Thermo. I_{sc} [mA]	Pyro. V_{oc} [V]	Pyro. I_{sc} [nA]
Sponge-confined	11.2	1.2	10	0.3	85	17
Free-flowing	6.2	0.7	5.0	0.28	4	9

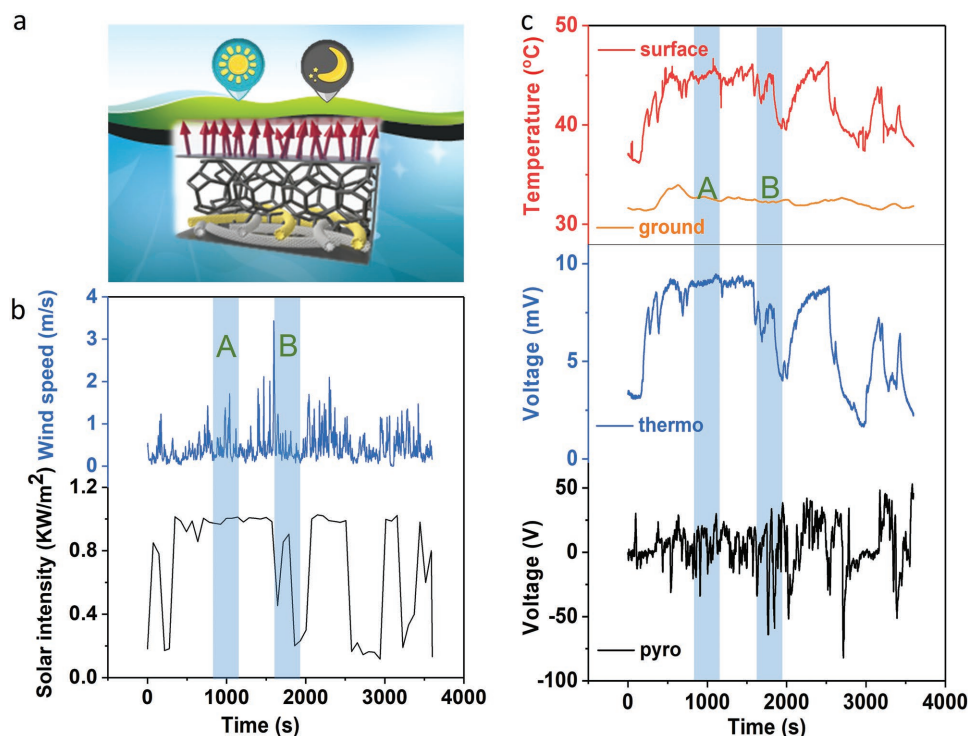


Figure 5. a) Sketch map of the hybrid photothermal generator in land, water, and night operation. b) Wind speed (blue curve) and solar intensity (black curve) depending on time of day during land operation. c) Temperature of the top surface of the generator (red curve) and beneath ground (yellow curve), V_{oc} of thermocell (blue curve) and pyroelectric generator (black curve). The outdoor test was carried out in NUS campus from 12:00 to 13:00 in April 12, 2018.

that of the hybrid generator with free-flowing electrolyte with a value of 0.86 mW m^{-2} . Meanwhile, the peak power output of the pyroelectric component of the hybrid generator with sponge-confined electrolyte is 0.9 mW m^{-2} , which is almost 40 times higher than $23 \text{ } \mu\text{W m}^{-2}$ for the hybrid generator with free-flowing electrolyte. These results clearly proved the essence of a sponge-confined electrolyte for an efficient hybrid photothermal thermogalvanic and pyroelectric generator.

To demonstrate the potential of practical application, a scaled-up hybrid generator with active area of $10 \text{ cm} \times 10 \text{ cm}$ was tested under unstructured outdoor environment for multisituation low grade heat harvesting as sketched in Figure 5a. To test the generating performance on ground under natural sunlight, the top surface of the generator was exposed to solar irradiation while the back side was placed close to the ground (inset in Figure S6, Supporting Information). The infrared image in Figure S6 (Supporting Information) clearly shows that the top surface of the cell is hotter than the surrounding. The time-dependent solar irradiance and wind speed are recorded in Figure 5b. The temperature of the top surface (red line in Figure 5c) and the ground underneath (yellow line in Figure 5c) were recorded by an infrared camera and thermocouple, respectively. The temperature of the ground under the device varied within a small range of $31.5\text{--}34 \text{ }^\circ\text{C}$ throughout the test. The temperature of the top surface, in contrast, fluctuated much more drastically and was highly receptive to the natural ambient conditions, such as the real-time solar intensity, wind as well as the roaming clouds. To further investigate the synergic roles played by the thermocell and pyroelectric generator,

two typical periods are marked in blue whereby period A is relatively steady while period B is more erratic. During the period A when solar irradiation is stable and intense, the temperature of the top surface is high and steady, thus leading to a high thermocell performance while the pyroelectric effect is modest. On the contrary, when the weather is unpredictably fluctuating during the period B, the hybrid cell accordingly experiences an irregular temperature variation, yielding a pronounced pyroelectric performance but a declined thermogalvanic effect. Notably, the irregular wind existed throughout the test process, resulting in an incessant pyroelectricity. Evidently, this showcases the significance of adaptiveness or responsiveness of the hybrid device to the ever-changing unstructured outdoor environments.

Furthermore, the hybrid cell was also tested on water surface, showing viable and augmented thermogalvanic and pyroelectric performance (Figure S7, Supporting Information). It is anticipated that the performance of both the thermocell and pyroelectric generator will further improve when the hybrid generators are deployed on large water bodies surfaces, where the bulk water is much cooler and the wind is much stronger. Therefore, such hybrid generator provides a new strategy for scavenging blue energy. And what is especially remarkable is that such hybrid generator also performs energy scavenging at night. The feasibility experiment of harvesting energy from the temperature difference between the ground and air at night has been successfully conducted as shown in Figure S8 (Supporting Information). Hence, such hybrid generator has potential to serve as an all-day power source regardless of the day-night alternation.

3. Conclusion

In summary, we have demonstrated a hybrid photothermal generator consisting of thermocell and pyroelectric generator for multisituation energy harvesting regardless of the ever-changing ambient and day/night conditions. The CNT/CNC nanocomposites effectively act as photoabsorber and electrodes exhibiting broadband solar absorption and high electrical conductivity. Additionally, enhanced solar-thermal conversion was achieved via heat localization effect of the porous sponge-confined thermogalvanic electrolyte. Thus, the hybrid generator has achieved simultaneously high thermogalvanic and pyroelectric performance under irradiation of 1 sun with maximum output as high as 1.86 and 0.9 mW m⁻², respectively. Finally, we demonstrated the potential of spatiotemporal waste heat to electricity conversion on land and water bodies at different day/night time and steady/erratic environment. This work suggests that such hybrid generator described here may offer a promising alternative to capture and recover renewable solar and blue energy for an all-day/continuous power supply.

4. Experimental Section

Experimental details and specific characterization methods are described in the Supporting Information.

Supporting Information

Supporting Information is available from the Wiley Online Library or from the author.

Acknowledgements

This research is supported by the Singapore Ministry of National Development and the National Research Foundation, Prime Minister's Office under the Land and Liveability National Innovation Challenge (L2 NIC) Research Programme (L2 NIC Award No. L2NICCFP2-2015-3).

Conflict of Interest

The authors declare no conflict of interest.

Keywords

low grade heat harvesting, photothermal, pyroelectric, thermogalvanic

Received: August 2, 2018

Revised: September 11, 2018

Published online: October 14, 2018

[1] H. Ghasemi, G. Ni, A. M. Marconnet, J. Loomis, S. Yerci, N. Miljkovic, G. Chen, *Nat. Commun.* **2014**, *5*, 4449.

[2] X. Hu, W. Xu, L. Zhou, Y. Tan, Y. Wang, S. Zhu, J. Zhu, *Adv. Mater.* **2017**, *29*, 1604031.

- [3] Q. Jiang, L. Tian, K. K. Liu, S. Tadeipalli, R. Raliya, P. Biswas, R. R. Naik, S. Singamaneni, *Adv. Mater.* **2016**, *28*, 9400.
- [4] G. Ni, G. Li, S. V. Boriskina, H. Li, W. Yang, T. Zhang, G. Chen, *Nat. Energy* **2016**, *1*, 16126.
- [5] H. Liu, C. Chen, G. Chen, Y. Kuang, X. Zhao, J. Song, C. Jia, X. Xu, E. Hitz, H. Xie, S. Wang, F. Jiang, T. Li, Y. Li, A. Gong, R. Yang, S. Das, L. Hu, *Adv. Energy Mater.* **2018**, *8*, 1701616.
- [6] L. Zhu, M. Gao, C. K. N. Peh, G. W. Ho, *Mater. Horiz.* **2018**, *5*, 323.
- [7] M. Gao, P. K. N. Connor, G. W. Ho, *Energy Environ. Sci.* **2016**, *9*, 3151.
- [8] X. Zhang, X. Lu, Y. Shen, J. Han, L. Yuan, L. Gong, Z. Xu, X. Bai, M. Wei, Y. Tong, Y. Gao, J. Chen, J. Zhou, Z. L. Wang, *Chem. Commun.* **2011**, *47*, 5804.
- [9] J. Wang, L. Zhu, G. Dharan, G. W. Ho, *J. Mater. Chem. A* **2017**, *5*, 16580.
- [10] M. Q. Yang, M. Gao, M. Hong, G. W. Ho, *Adv. Mater.* **2018**, <https://doi.org/10.1002/adma.201802894>.
- [11] M. Wang, X. Pang, D. Zheng, Y. He, L. Sun, C. Lin, Z. Lin, *J. Mater. Chem. A* **2016**, *4*, 7190.
- [12] M. Wang, D. Zheng, M. Ye, C. Zhang, B. Xu, C. Lin, L. Sun, Z. Lin, *Small* **2015**, *11*, 1436.
- [13] Y. Hu, Z. Li, T. Lan, W. Chen, *Adv. Mater.* **2016**, *28*, 10548.
- [14] X. Yu, J. Pan, J. Deng, J. Zhou, X. Sun, H. Peng, *Adv. Mater.* **2016**, *28*, 10744.
- [15] X. Q. Wang, C. F. Tan, K. H. Chan, K. Xu, M. Hong, S. W. Kim, G. W. Ho, *ACS Nano* **2017**, *11*, 10568.
- [16] P. Yang, K. Liu, Q. Chen, J. Li, J. Duan, G. Xue, Z. Xu, W. Xie, J. Zhou, *Energy Environ. Sci.* **2017**, *10*, 1923.
- [17] M. He, B. Li, X. Cui, B. Jiang, Y. He, Y. Chen, D. O'Neil, P. Szymanski, M. A. Ei-Sayed, J. Huang, Z. Lin, *Nat. Commun.* **2017**, *8*, 16045.
- [18] X. Zhang, Z. Yu, C. Wang, D. Zarrouk, J. W. Seo, J. C. Cheng, A. D. Buchan, K. Takei, Y. Zhao, J. W. Ager, J. Zhang, M. Hettick, M. C. Hersam, A. P. Pisano, R. S. Fearing, A. Javey, *Nat. Commun.* **2014**, *5*, 2983.
- [19] Y. Tai, G. Lubineau, Z. Yang, *Adv. Mater.* **2016**, *28*, 4665.
- [20] H. Cheng, F. Zhao, J. Xue, G. Shi, L. Jiang, L. Qu, *ACS Nano* **2016**, *10*, 9529.
- [21] J. Deng, J. Li, P. Chen, X. Fang, X. Sun, Y. Jiang, W. Weng, B. Wang, H. Peng, *J. Am. Chem. Soc.* **2016**, *138*, 225.
- [22] Y. Hu, G. Wu, T. Lan, J. Zhao, Y. Liu, W. Chen, *Adv. Mater.* **2015**, *27*, 7867.
- [23] W. Jiang, D. Niu, H. Liu, C. Wang, T. Zhao, L. Yin, Y. Shi, B. Chen, Y. Ding, B. Lu, *Adv. Funct. Mater.* **2014**, *24*, 7598.
- [24] X. Q. Wang, C. F. Tan, K. H. Chan, X. Lu, L. Zhu, S. W. Kim, G. W. Ho, *Nat. Commun.* **2018**, *9*, 3438.
- [25] D. Kraemer, B. Poudel, H. P. Feng, J. C. Caylor, B. Yu, X. Yan, Y. Ma, X. Wang, D. Wang, A. Muto, K. McEnaney, M. Chiesa, Z. Ren, G. Chen, *Nat. Mater.* **2011**, *10*, 532.
- [26] L. Xu, Y. Xiong, A. Mei, Y. Hu, Y. Rong, Y. Zhou, B. Hu, H. Han, *Adv. Energy Mater.* **2018**, *8*, 1702937.
- [27] C. R. Bowen, J. Taylor, E. LeBoulbar, D. Zabek, A. Chauhan, R. Vaish, *Energy Environ. Sci.* **2014**, *7*, 3836.
- [28] S. Wang, Z. L. Wang, Y. Yang, *Adv. Mater.* **2016**, *28*, 2881.
- [29] T. Park, J. Na, B. Kim, Y. Kim, H. Shin, E. Kim, *ACS Nano* **2015**, *9*, 11830.
- [30] L. E. Bell, *Science* **2008**, *321*, 1457.
- [31] K. Liu, T. Ding, J. Li, Q. Chen, G. Xue, P. Yang, M. Xu, Z. L. Wang, J. Zhou, *Adv. Energy Mater.* **2018**, *8*, 1702481.
- [32] R. Hu, B. A. Cola, N. Haram, J. A. Barisci, S. Lee, S. Stoughton, G. Wallace, C. Too, M. Thomas, A. Gestos, M. E. Cruz, J. P. Ferraris, A. A. Zakhidov, R. H. Baughman, *Nano Lett.* **2010**, *10*, 838.
- [33] T. Kim, J. S. Lee, G. Lee, H. Yoon, J. Yoon, T. J. Kang, Y. H. Kim, *Nano Energy* **2017**, *31*, 160.

- [34] P. Yang, K. Liu, Q. Chen, X. Mo, Y. Zhou, S. Li, G. Feng, J. Zhou, *Angew. Chem., Int. Ed.* **2016**, *55*, 12050.
- [35] M. F. Dupont, D. R. MacFarlane, J. M. Pringle, *Chem. Commun.* **2017**, *53*, 6288.
- [36] S. Beck-Candanedo, M. Roman, D. G. Gray, *Biomacromolecules* **2005**, *6*, 1048.
- [37] W. Luo, J. Hayden, S.-H. Jang, Y. Wang, Y. Zhang, Y. Kuang, Y. Wang, Y. Zhou, G. W. Rubloff, C.-F. Lin, L. Hu, *Adv. Energy Mater.* **2018**, *8*, 1702615.
- [38] M. M. Hamed, A. Hajian, A. B. Fall, K. Hakansson, M. Salajkova, F. Lundell, L. Wagberg, L. A. Berglund, *ACS Nano* **2014**, *8*, 2467.
- [39] C. Chen, Y. Li, J. Song, Z. Yang, Y. Kuang, E. Hitz, C. Jia, A. Gong, F. Jiang, J. Y. Zhu, B. Yang, J. Xie, L. Hu, *Adv. Mater.* **2017**, *29*, 1701756.
- [40] Y. Li, T. Gao, Z. Yang, C. Chen, W. Luo, J. Song, E. Hitz, C. Jia, Y. Zhou, B. Liu, B. Yang, L. Hu, *Adv. Mater.* **2017**, *29*, 1700981.
- [41] M. Al Maimani, J. J. Black, L. Aldous, *Electrochem. Commun.* **2016**, *72*, 181.
- [42] Y. Fu, G. Wang, T. Mei, J. Li, J. Wang, X. Wang, *ACS Sustainable Chem. Eng.* **2017**, *5*, 4665.
- [43] L. Zhu, M. Gao, C. K. N. Peh, X. Wang, G. W. Ho, *Adv. Energy Mater.* **2018**, *8*, 1702149.
- [44] N. Xu, X. Hu, W. Xu, X. Li, L. Zhou, S. Zhu, J. Zhu, *Adv. Mater.* **2017**, *29*, 1606762.
- [45] C. Jia, Y. Li, Z. Yang, G. Chen, Y. Yao, F. Jiang, Y. Kuang, G. Pastel, H. Xie, B. Yang, S. Das, L. Hu, *Joule* **2017**, *1*, 588.
- [46] G. Xue, K. Liu, Q. Chen, P. Yang, J. Li, T. Ding, J. Duan, B. Qi, J. Zhou, *ACS Appl. Mater. Interfaces* **2017**, *9*, 15052.